Eladl *et al. Journal of Electric Propulsion* (2026) 5:11
https://doi.org/10.1007/s44205-026-00186-w

Journal of Electric Propulsion

RESEARCH **Open Access**

High current density operation of a 4.5-kW Hall effect thruster on krypton

Muhannad Eladl[1*], Nicolas Montero[1], Chhavi Chhavi[1], Dan Lev[1], Mitchell L. R. Walker[1], Bao Nguyen[2], Amy Cichan[2] and Steven Shepard[2]

*Correspondence:
Muhannad Eladl
meladl3@gatech.edu
[1]Georgia Institute of Technology, Atlanta, Georgia 30332, USA
[2]Lockheed Martin, Bethesda, MD 20817, USA

Abstract

The high current density operation of the 4.5-kW T-140 Hall effect thruster, is characterized on krypton at operating powers up to approximately 2.5x the nominal power. Nominal operating setpoints are identified and characterized at discharge currents of 8 to 10 A and discharge voltage of 300 V, 2.4–4.5 kW. The thruster performance is characterized at high current density operation varying the discharge current from 10 to 20 A in 2-A steps at three different discharge voltages: 300, 400, and 500 V. The global performance is characterized, with a specific focus on the anode efficiency, for high current density operation and to understand the effect of varying discharge voltage on the operating conditions. The 300 V condition exhibits a peak anode efficiency of 49% at 14 A. The 400 and 500 V conditions demonstrate increasing anode efficiency with discharge current that approaches an asymptote of approximately 56% and 60% respectively. The anode efficiency is decomposed into constituent efficiencies, individually characterized based on plasma properties measured in the plume in order to gain a better understanding of the physics underlying the measured behavior. The current utilization efficiency is the lowest efficiency and the observed trends match those seen in the overall anode efficiency, suggesting that it has the greatest effect on the measured efficiency behavior. The mass utilization and divergence efficiencies also vary significantly with both discharge voltage and current, with a peak difference of 13% and 7%, respectively, across the tested range. Meanwhile, the voltage utilization shows small increases with discharge voltage and no discernible pattern with discharge current. The uncertainty in the total anode efficiency was calculated to be ± 5–7% of the reported value. Neglecting multiply-charged ions is a potential source of error, but a comparison between the anode efficiency measurements based on thrust and the anode efficiency estimates based on plume measurements shows that the difference between the two methods is within the aforementioned uncertainty of the anode efficiency for all setpoints giving confidence in the analysis methods employed.

Keywords High Current Density, T140 Hall Effect Thruster, Anode Efficiency, RPA, Langmuir, Faraday

Introduction

Over the last few decades there has been a shift to the use of more electric propulsion (EP) thrusters for in-space applications, with some missions, such as the Boeing 702SP and the Eurostar E3000, using EP as their only propulsion system [1]. As the capabilities of energy production and storage systems have increased, more ambitious deep-space missions have become feasible, and hence there has been a push for higher thrust capabilities and higher power propulsion devices [2]. Operating EP devices at higher thrust densities can produce these higher thrust requirements with a physically smaller thruster envelope and mass [3]. State-of-the art Hall effect thrusters (HETs) operate at high thrust densities when compared to similarly developed EP technologies. With only magentoplasmadynamic thrusters (MPDTs), which are at a lower technology readiness level (TRL), having higher capabilities; HETs are an attractive choice for missions with high thrust requirements [3].

Despite the high thrust densities of state-of-the art HETs relative to comparative technologies, an analysis by Simmonds et al. has shown that the theoretical limit on HET thrust density is orders of magnitude higher than present capabilities [3]. However, efforts to increase the thrust density have proven difficult. Previous efforts have included increasing discharge voltage at a constant current density [3] or concentrically nesting multiple discharge channels [4] leading to either marginal improvements in the thrust density or losses in performance. One method to increase thrust density is to increase the current density by increasing the discharge current without increasing the physical size of the thruster. Su et al. operated a magnetically shielded 9-kW HET, the H9, on krypton and xenon at beam currents up to 10x the "nominal" setpoint and measured a 5x increase in thrust density [5]. The anode and total efficiencies reached a maximum value with further increases in current density leading to decreases in efficiency for operation on xenon but monotonically increased towards an asymptote for operation on krypton. The works of Lev et al. characterized the high-power density operation of a 200–300 W thruster on xenon at powers up to 3x the "nominal" setpoint at various discharge voltages measuring a thrust density increase of up to 3x [6]. The anode efficiency shows a similar trend with discharge seen in the H9 xenon operation, with peak efficiencies measured for the 300 and 400 V discharge conditions. The test highlights some of the potential difficulties with operating at high-current densities at various discharge voltages as a steady discharge could not be sustained at the full range of discharge powers at 200, 500, and 600 V discharge conditions.

The purpose of this paper is to continue understanding the performance of high-power HETs for high current density operation. In this work, the efficiency of a 4.5-kW HET operating on krypton is investigated with increasing discharge current at three discharge voltage conditions. Measurements of the plasma properties in the plume are used to understand how the efficiency changes with current density and discharge voltage. Previous work done on krypton analyzed the changes in efficiency with discharge current for high current density operation of a magnetically shielded HET [5]. This work will analyze the efficiency trends with discharge current for the high current density operation of an unshielded thruster and investigate how these trends change with varying discharge voltage. While Lev et al. did attempt to analyze high current density operation at different discharge voltages, this work was done for a sub-kW thruster operating on xenon [6]. Furthermore, due to the instability of the thruster at certain discharge conditions, clear trends with discharge voltage could not be discerned.

It is important to note that most state-of-the-art HETs are magnetically shielded due to their lower erosion, which is expected to increase at higher current densities [5]. However, magnetically shielded HETs have been shown to exhibit a large increase in current oscillations at high voltages that are much less severe in unshielded thrusters [37, 38]. The reason behind this mode transition appearing in the magnetically shielded configuration but not the unshielded configuration is not fully understood [37, 38]. While increasing current density has been shown to dampen the oscillations for operation on xenon, this effect has been shown to be lower for krypton operation with current oscillations even increasing again at very high current densities [5]. As such, unshielded thrusters may be advantageous for certain operation regimes and their performance is worth investigating.

The manuscript is organized as follows: Section "Experimental setup" describes the experimental setup including the test article, operating conditions, facility, and diagnostics employed. Section "Performance analysis" outlines the analysis framework used to calculate the anode efficiency breakdown from probe measurements as well as a method for accounting for neutral ingestion. Section "Results and discussion" presents the results of the experiment alongside a discussion of the physical processes behind these results. Section "Scaling laws and nondimensional analysis" compares the results obtained from this investigation to scaling laws and non-dimensional parameters derived in previous works.

Experimental setup

In this section we describe the test setup, providing details of both the test article and operational setpoints. This section also details the facility used for testing and the diagnostics that were employed.

Test article

The test article used for this experiment was a T-140 HET, shown in Fig. 1, with a target setpoint of 4.5 kW and a nominal operating range of 2.4–4.5 kW on xenon [7, 8]. The thruster has a stainless-steel anode and an M26 boron nitride discharge channel with

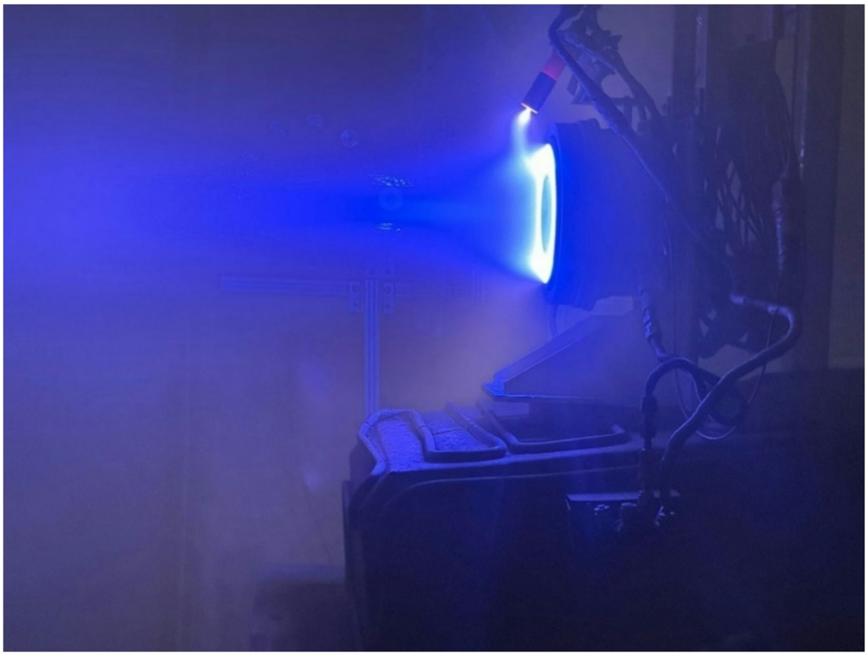

Fig. 1 T-140 operating on krypton at 300 V and 16 A

a 143 mm diameter [8]. No major modifications were made to the thruster for this test. We used an EPL-500 cathode, produced by Electric Propulsion Inc., chosen for its ability to supply up to 50 A of current, which allows ample current for the high-current density setpoints.

Operating setpoints

Table 1 presents the operating setpoints for this test. The T-140 is nominally operated on xenon at a discharge voltage range of 250 to 450 V and a discharge current range of 7–10 A [7, 8]. As the T-140 was operated on krypton instead of xenon for this test, it is important to define the "nominal" test conditions. Given that the main variable is the discharge current, for this paper we define the nominal setpoints based on discharge current setpoints that the T-140 was designed for and operated at in the past [7]. The experiment was conducted at three discharge voltage conditions, 300, 400 and 500 V, and three nominal discharge current setpoints, 8, 9, and 10 A, at each voltage as a baseline for the test. The discharge current was then increased up to 20 A in 2-A steps for each voltage condition. The cathode was operated at 10% ± 1% of the anode mass flow rate, as this provided the most stable thruster operation at the nominal setpoints, determined by minimizing peak-to-peak oscillations in the discharge current.

The T140 has operated at multiple magnetic field topologies in previously published experiments [7]. For this experiment, the inner magnet coil was operated at 13.1 A and the outer magnet coil was operated at 12.0 A, which, out of the aforementioned topology configurations, provided the maximum stability at the nominal power setpoints. The magnet currents were kept constant for all setpoints.

Measurements were taken at each setpoint after the thruster had reached thermal steady state. This was determined using a thermocouple measurement of the thruster

Table 1 Thruster operating setpoints

Discharge Voltage, V	Discharge Current, A	Anode Mass Flow, mg/s	Operating Pressure, μ Torr
300	8	5.71	11.3
300	9	6.25	12.7
300	10	7.31	14.7
300	12	8.29	19.9
300	14	9.63	24.8
300	16	10.57	30.2
300	18	11.51	35.3
300	20	12.43	38.1
400	8	5.74	10.4
400	9	6.53	14.4
400	10	7.43	16.3
400	12	8.52	22.5
400	14	9.67	27.4
400	16	10.88	30.4
400	18	11.97	33.6
400	20	13.19	36.9
500	9	6.48	12.2
500	10	7.18	15.4
500	12	8.52	21.7
500	14	9.79	25.3
500	16	10.69	32.1
500	18	11.77	36.7
500	20	12.99	38.8

body temperature. The thruster was ignited at 9 A at the setpoint discharge voltage, after which the discharge current was ramped up to the setpoint over a 5–10 min period. The thruster was then operated at the intended condition until the rate of change of the temperature measurement was less than 0.2^{o} C per minute. This process took about 1–1.5 h depending on the setpoint. The 500 V, 8 A discharge condition could not be operated steadily long enough without the plasma extinguishing to reach this condition and as such data for that setpoint could not be taken.

Facility

The experiment was conducted in a 7-m-long by 4-m-diameter stainless steel vacuum chamber, shown in Fig. 2. The chamber is operated using two rotary vane pumps and six diffusion pumps with a combined pumping capacity of 600,000 l/s on air and 240,000 l/s on krypton. The chamber reaches a base pressure of 2.5 μTorr ± 1 μTorr. The pressure in the chamber is measured using a Varian type 571 hot filament ion gauge mounted on the side of the chamber. The thruster is placed on a thrust stand approximately 5.5 m from the downstream end of the chamber axially. Figure 2 depicts a set of plasma probes mounted on a rotary stage placed 1 m downstream of the thruster exit plane, and enables plasma properties in the thruster plume to be measured in an arc. A slated graphite beam dump located axially downstream of the thruster ensures neutrals and any non-neutralized ions do not rebound back towards the thruster. It also acts as a barrier to prevent energetic ions exiting the thruster from impinging on and damaging the downstream chamber wall. Graphite is chosen as the material for the beam dump due to its very low sputter rate. A 100 and 1000 sccm calibrated mass flow controller supplies the gas flow to the cathode and anode, respectively, with a reported uncertainty of ±1% of the reading.

Diagnostics

A variety of diagnostic probes were used to characterize both the thruster performance and the plasma properties of the plume. The discharge current and voltage of the thruster were measured using a Teledyne Lecroy CP 150 current probe and a Powertek DP25 differential voltage probe connected to an HDO6104 oscilloscope. The discharge

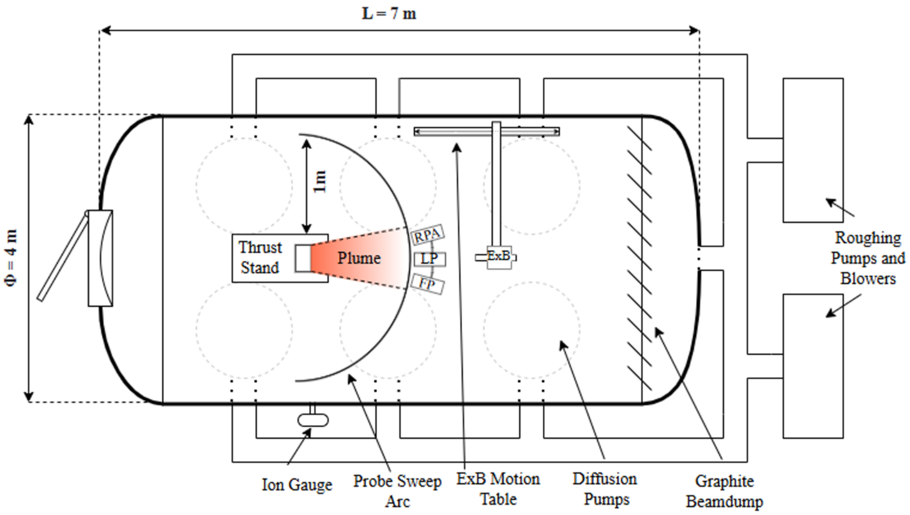

Fig. 2 Vacuum chamber schematic

properties were sampled at a rate of 10 MHz, and a running average was applied to get mean values of the properties. The thruster sits on a thrust stand, used to make calibrated thrust measurements in order to characterize the performance properties of the thruster. Faraday, Langmuir, and RPA probes are all mounted on the aforementioned rotary arm allowing for spatially resolved plasma measurements in the plume of the thruster. All probes were placed in a graphite housing, which protected the probes and their wiring as well as minimized sputtering off of and onto the probe surfaces. A thermocouple is placed on the thruster body to measure body temperature at each setpoint.

Thrust stand

The thrust stand employed is an inverted pendulum based on the design presented by Polk et al. [9]. A linear variable differential transformer (LVDT) measures the deflection of the thrust stand due to an applied force and outputs a proportional DC bias. The DC bias is processed by a PID controller and an electromagnetic coil applies a force in the opposite direction until the LVDT output is zero. The current required by the coil to apply the aforementioned force is measured as the thrust signal. A set of calibration weights is loaded onto the stand using a motorized pulley system, applying a set of known forces that can be used to interpret the current signal output of the thrust stand into an actual force. This calibration process is repeated after each thrust measurement to account for any drift in the output signal with time. The thrust stand electronics are kept at a constant temperature using a chiller system to minimize thermal-related drift. Uncertainty in the thrust measurements is based on the systematic drift of the system, accounted for in the calibration process, and the random error is quantified based on three repeat measurements.

Langmuir probe

The first plasma diagnostic employed on the rotary stage is a Langmuir probe, which provides spatially resolved plasma potential, electron density, and electron temperature, as well as ion and electron saturation voltages and currents. For this experiment, a cylindrical Langmuir probe with a tungsten wire of 0.13 mm diameter and a 6 mm length serving as the electrode tip is employed. The tip is housed in a cylindrical alumina rod with a 6.5 mm diameter and 65 mm length. A Keithley 2470 SourceMeter both applied the voltage to and measured the current collected on the probe's tungsten tip. The voltage was swept from − 50 V to 100 V in 0.25-V increments. The Langmuir probe measurements are taken at the thruster centerline. The measured I-V curves are analyzed using the theory presented by Lobbia et al. [10]. in order to extract the relevant plasma properties.

Faraday probe

A nude-type JPL Faraday probe, as described in the works of Hofer et al., is used to measure the ion current density [11]. The probe consists of a cylindrical collector, with a diameter of 2.31 cm and a thickness of 0.62 cm, and a cylindrical guard ring with an outer diameter of 2.54 cm and a wall thickness of 0.074 cm. A 0.036-cm gap separates the collector and the guard ring, and care is taken to ensure that the resistance between the two is greater than 1 MΩ. The purpose of the guard ring is to prevent the collection of ions outside of the projected area of the collector face. Both the guard and the collector are made from stainless steel and the collector has a tungsten coating to minimize secondary electron emission. A ceramic spacer sits between the collector and the shield to help maintain the required isolation between the two components. The Faraday probe is swept from – 90° to 90° at a constant rate of 2 degrees/s using the rotary arm. The probe is held at a constant voltage of -30 V, and a Keithley 2470 SourceMeter collects the current as the probe sweeps through the plume with a positional resolution of 0.2°. The ion beam current, I_b, and the divergence angle, θ_{div}, are calculated using the data reduction scheme presented in the works of Brown et al. [12]. The methods employed to account for charge exchange and neutral ingestion are discussed in Sec. II.C.

RPA probe

A Retarding Potential Analyzer (RPA) is used to measure the ion velocity distribution function. The RPA consists of four electrostatically biased grids: a floating grid to minimize perturbations to the plasma caused by the probe, a negatively biased electron repulsion grid to repel electrons from the plasma, an ion repulsion grid with a variable bias used to repel high-energy ions based on the applied bias, and a negatively biased electron suppression grid used to repel secondary electron emissions coming off the collector. Both the electron repulsion and suppression grids are biased to -30 V. A Keithley 2470 SourceMeter sweeps the voltage of the ion repulsion grid from 0 to 500 V in 1-V increments while simultaneously measuring the current from the collector. The negative numerical derivative of the resulting I-V curve, yields the ion energy distribution function. Initially, RPA measurements were taken at multiple rotary stage positions, but only measurements at the thruster centerline have a sufficient signal-to-noise ratio for analysis.

Thermocouple

A K-type thermocouple was placed on the side of the thruster body. Temperature measurements were taken with an accuracy of ± 2° C.

Performance analysis

The following section outlines the analysis procedure used to calculate the performance parameters based on the diagnostic measurements taken, as described in the previous section. This section also includes a description of the necessary corrections to account for neutral ingestion and background pressure.

Global performance metrics

The main global parameters relevant to this work are the thrust, specific impulse and anode efficiency. The thrust is measured directly using the thrust stand as described in the diagnostics section. The specific impulse and anode efficiency are defined as:

$$I_{sp} = \frac{T}{\dot{m}g_o}\,(1) \tag{1}$$

$$\eta_a = \frac{T^2}{2\dot{m}_a P_d} \tag{2}$$

where I_{sp} is specific impulse, T is thrust, $\dot{m}$ is the total mass flow rate, g_o is standard gravity, η_a is anode efficiency, $\dot{m}_a$ is the anode mass flow rate, and P_d is discharge power. The analysis in this paper will focus on anode efficiency, which only accounts for discharge power, instead of total efficiency, which accounts for the power consumed by all subsystems of the thrusters, such as the magnets. The power consumption of subsystems such as magnets are heavily dependent on their manufacturing, which often differs greatly between different lab modules and between lab modules and flight hardware. As such, considering anode efficiency allows the analysis to focus on the effects of the discharge and plume of the thruster.

Efficiency decomposition

In order to understand the underlying mechanisms behind the results, the anode efficiency is decomposed into constituent efficiencies that are dependent on the thruster's ionization and acceleration processes [13]:

$$\eta_a = \eta_q \eta_v \eta_b \eta_d \eta_m \tag{3}$$

where η_q is the charge utilization efficiency, η_v is the voltage utilization efficiency, η_b beam utilization efficiency, η_d is the divergence efficiency and η_m is the mass utilization efficiency. Each of the constituent efficiencies can be calculated using probe measurements of the plume.

The charge utilization efficiency accounts for the inefficiencies that arise from the production of multiply charged ions and can be defined as:

$$\eta_q = \frac{\left(\sum \Omega_i/\sqrt{Z_i}\right)^2}{\sum \Omega_i/Z_i} \tag{4}$$

where Ω_i is the current fraction of the i^{th} ion species and Z_i is the charge of the i^{th} ion species. The fraction of each species is normally characterized using an ExB probe; however, we were unable to get resolvable measurements for this experiment. Previous experiments show that the effect of charge utilization is small for HETs operating on krypton and has little variation with increasing discharge current with values ranging from 0.95 to 0.99 [5]. However, the characterization of the charge utilization efficiency is an area for improvement for future work.

The voltage utilization accounts for inefficiencies in the conversion of discharge voltage to the accelerating voltage of ions for thrust production and can be defined as:

$$\eta_v = \frac{V_a}{V_d} \tag{5}$$

where V_a is the acceleration voltage experienced by ions and V_d is the discharge voltage. This efficiency is characterized based on the ion energy distribution measurement of the RPA.

The current utilization efficiency accounts for the fraction of discharge current that enters the plumes as beam current. It can be defined as:

$$\eta_b = \frac{I_b}{I_d} \tag{6}$$

where I_b is the ion beam current and I_d is the discharge current. The current utilization efficiency is characterized using beam current measurements from the Faraday probe.

The divergence efficiency accounts for losses that occur due to the non-axial component of the momentum of ions leaving the thruster not imparting thrust. It can be defined as:

$$\eta_d = (\cos(\theta_d))^2 \tag{7}$$

where θ_d is the divergence angle measured using the Faraday probe.

The mass utilization efficiency accounts for losses that occur when converting the neutral gas input into the thrust into ion flux and can be defined as:

$$\eta_m = \frac{\dot{m}_b}{\dot{m}_a} = \frac{m_p I_b}{q_e \dot{m}_a} \tag{8}$$

where $\dot{m}_b$ is the ion beam mass flow rate, $\dot{m}_a$ is the anode mass flow rate, m_p is the mass of the propellant atom, and q_e is the elementary charge of an electron. The ion beam flow rate can be calculated based on Faraday probe measurements. It is important to note that Eq. (8) assumes all ions are singly charged. The effect of this assumption on the results will be discussed later.

Neutral ingestion and background pressure corrections

As the flow rate increased for the higher current setpoints, the operating pressure in the chamber increased as well making it important to account for the effect of ingested neutrals for accurate estimates of thrust and efficiency. Nominally, the effects of neutral ingestion are accounted for by taking measurements with varied chamber pressure and extrapolating to a perfect vacuum. However, given the high operating pressure for the setpoints tested, this method is not feasible. Instead, the effect of neutral ingestion was corrected for using the model outlined in the works of Randolph [14] and Brown [15]. In this model, the neutral mass flow into the thruster was calculated based on an approximated hemispherical entrainment area encompassing the outer diameter of the thruster discharge:

$$\dot{m}_{en} = A_{en} p \left(\frac{m_p}{2\pi k_b T_o} \right)^{1/2} \tag{9}$$

where $\dot{m}_{en}$is the entrained neutral mass flow rate, A_{en} is the aforementioned hemispherical entrainment area, p is the operating pressure of the pressure at a given setpoint, k_b is Boltzmann's constant, and T_o is the neutral gas temperature, which is assumed to be 300 K for this work. While the entrained neutrals are assumed to be ionized and accelerated, the acceleration experienced by ingested neutrals is not the same as that of the neutrals originating from the anode; as such, empirically derived factors for the entrainment area and thrust are introduced to account for this. The resulting corrected discharge current, thrust, and beam current are:

$$I_{d,corr} = I_d - \zeta_A \dot{m}_{en} \frac{q_e}{m_p} \tag{10}$$

$$T_{corr} = T(1 - \zeta_{en}\frac{\dot{m}_{en}}{\dot{m}_{en} + \dot{m}_a}) \tag{11}$$

$$I_{b,corr} = I_b - \zeta_A \dot{m}_{en}\frac{q_e}{m_p} \tag{12}$$

where $I_{d,corr}$, $T_{,corr}$, $I_{b,corr}$ are the corrected discharge current, thrust, and beam current respectively, ζ_A is the empirical area entrainment correction factor, and ζ_{en} is the empirical thrust entrainment correction factor. ζ_A primarily accounts for deviations of the empirical results from the model at low discharge voltage operation [15], and as such, for this work it was set to 1 for all setpoints. ζ_{en} varies from 0 to 1, with $\zeta_{en} = 0$ meaning that none of the entrained neutrals contributed to useful thrust and the thrust remains uncorrected and $\zeta_{en} = 1$ meaning that all the entrained neutrals contributed to useful thrust and must be corrected for [15, 16]. As previously mentioned, the high operating pressure of the facility during this test prevents the required extrapolation to calculate ζ_{en}. As such, ζ_{en} was chosen for each point based on the power and mass flow scaling seen in the results of Brown and Reid [15, 16]. To account for potential errors from the choice of ζ_{en}, the uncorrected and fully corrected ($\zeta_{en} = 0$ and $\zeta_{en} = 1$ respectively) thrust values are calculated and included in the uncertainty bars.

Another effect of the higher operating pressure is the creation of charge exchange (CEX) ions, which can be an additional source of error in the calculations of ion beam current. These CEX ions arise when high energy ions collide with slower moving background gas; ionizing them and producing an artificial population of slower moving ions that are scattered to the periphery of the plume [12]. If uncorrected for, the CEX ions will lead to an artificially elevated measurement of current density at the periphery of the Faraday probe measurements, which leads to an erroneous estimation of the divergence angle [12]. The works of Hofer et al. [17]. and Azziz [18] outline a correction method that assumes the effect of CEX is the same spatially for the entire probe sweep and that the current collected at the wings of the plume is entirely due to CEX ions. As such, the effect of CEX can be accounted for by subtracting the current collected at the ends of the sweep, i.e. ± 90 degrees for the rotary stage, from the entire Faraday scan. However, laser induced fluorescence measurements on a 12.5 kW HET performed by Huang et al. have shown a non-negligible presence of higher energy ions at the wings of the plume [19]. Therefore, assuming that all current collected at ±90 degrees is due to CEX is an overcorrection that underestimates the beam current. Given there are multiple methods to account for CEX ions with varying degrees of over and under correction [12, 17, 18], for the purposes of this work the corrected beam current given by Eq. (12) is taken as the observed value with the uncorrected beam current taken as the upper uncertainty bound and the result of the aforementioned subtraction method taken as the lower uncertainty bound, as it overcorrects the most.

Results and discussion

The following section presents the results from the experiment alongside a discussion of the implications and potential physics behind these results. This analysis includes the efficiency breakdown presented in the previous section.

Global performance

Figure 3 shows the measured thrust as a function of discharge current discharge voltages of 300 V, 400 V, and 500 V. The thrust increases approximately linearly with discharge current as seen in previous measurements on krypton [5]. The results align with the fact that thrust increases linearly with mass flow rate because the discharge current is proportional to the mass flow rate. The measurements show that the thrust increases approximately with the square root of the discharge voltage as expected based on simplified analytical expressions [20]. Assuming all ions exiting the thruster are singly ionized, the thrust produced by a HET can be approximated as [20]:

$$T = \sqrt{\frac{2m_i}{q_e}} I_b \sqrt{V_a} \tag{13}$$

where m_i is the mass of the ion. This theoretical approximation's scaling for beam current and ion accelerating voltage, which approximately scale with discharge current and discharge voltage, matches the aforementioned trends in the measured thrust.

Figure 4 shows the specific impulse as a function of discharge current. For all three discharge voltages, the specific impulse initially increases with discharge current before reaching an asymptote, similar to trends previously seen on high current density tests with krypton [5]. The specific impulse also increases with discharge voltage scaling, similar to thrust, with the square root of discharge voltage. Furthermore, the asymptotic behavior is delayed, occurring at higher discharge currents, for the higher discharge voltage setpoints. The specific impulse can be approximated as [20]:

$$I_{sp} = \frac{\eta_m}{g_o} \sqrt{\frac{2q_e V_a}{m_i}} \tag{14}$$

This theoretical approximation scales with the square of accelerating voltage, which in turn scales approximately with discharge voltage, matching the trends seen in the measured data (Fig. 4). The approximation also scales with the mass utilization, which can be

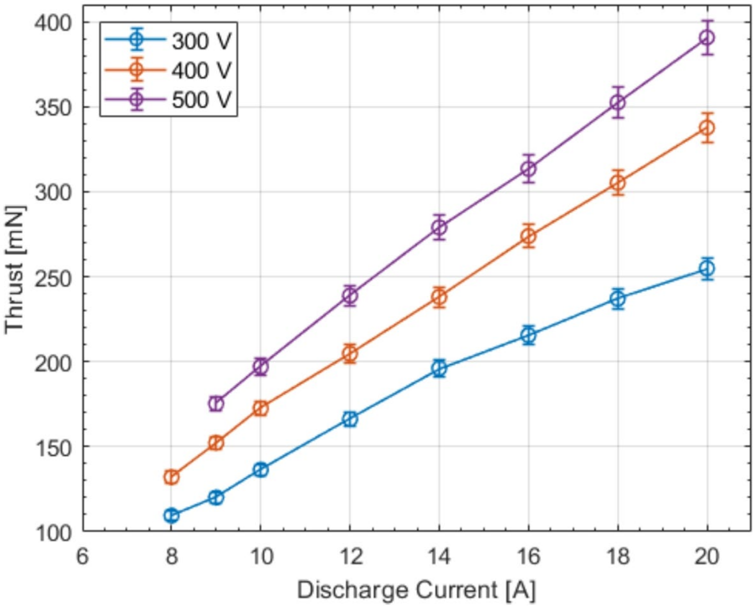

Fig. 3 Thrust as a function of discharge current for discharge voltages of 300 V, 400 V, and 500 V

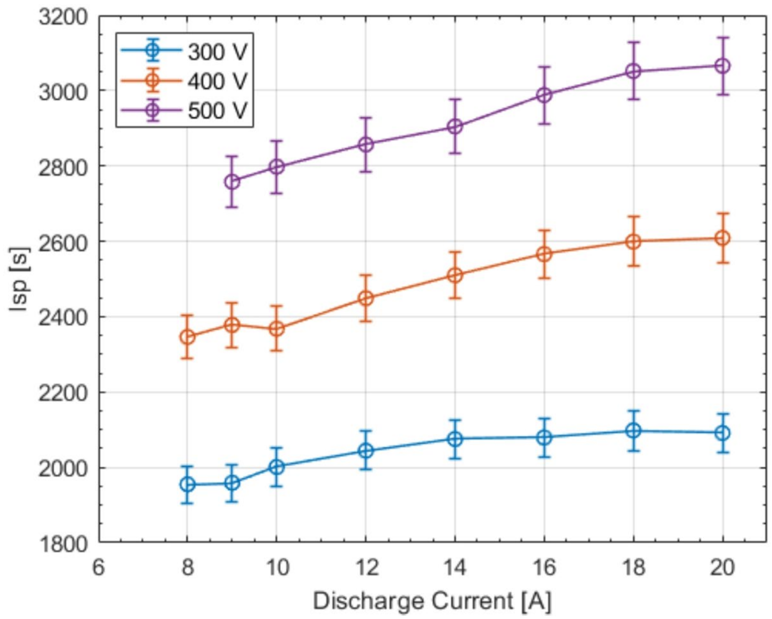

Fig. 4 Specific impulse as a function of discharge current for discharge voltages of 300 V, 400 V, and 500 V

used to understand the asymptotic behavior observed. This will be discussed further in Section "Efficiency breakdown analysis".

Figure 5 presents the anode efficiency as a function of discharge current. The 300 V discharge condition shows a distinct peak efficiency at 14 A discharge current, while the 400 and 500 V discharge conditions do not have a peak within the range of discharge currents tested and instead exhibit asymptotic behavior with increasing discharge current, with the expectation that the efficiency will peak at a higher discharge current outside of the tested range given the trend at 300 V. The efficiency increased with discharge voltage. Varying the discharge from 300 to 400 V exhibits a higher increase in efficiency relative to increasing the discharge voltage from 400 to 500 V. The peak anode efficiency was measured to be 59% ± 1.5% at 500 V and 20 A discharge conditions. The implications and potential reasoning behind the trends seen in anode efficiency will be discussed further when looking at the efficiency breakdown based on probe measurements.

Figure 6 shows the thrust-to-power ratio as a function of discharge current. The thrust-to-power ratio decreases with discharge voltage, approximately scaling by the inverse of the square root of voltage, as expected [20]. Interestingly, the thrust-to-power ratio exhibits a peak at 14 A for the 300 V condition following a similar trend to the anode efficiency. No peak is discernible outside of the uncertainty for the other conditions.

Probe measurements

In order to understand the trends in the measured global performance of the thruster, specifically anode efficiency, we utilize probe measurements of plasma parameters. Faraday probe measurements were taken to characterize the beam current and divergence of the plume. Figure 7 shows a representative trace of the raw Faraday probe measurements, while the resulting ion beam currents and ion beam divergence angles are presented in Figs. 8 and 9, respectively.

As the discharge current increases, the measured peak current increases, suggesting a larger beam current, which is reflected in the results shown in Fig. 8. The measured

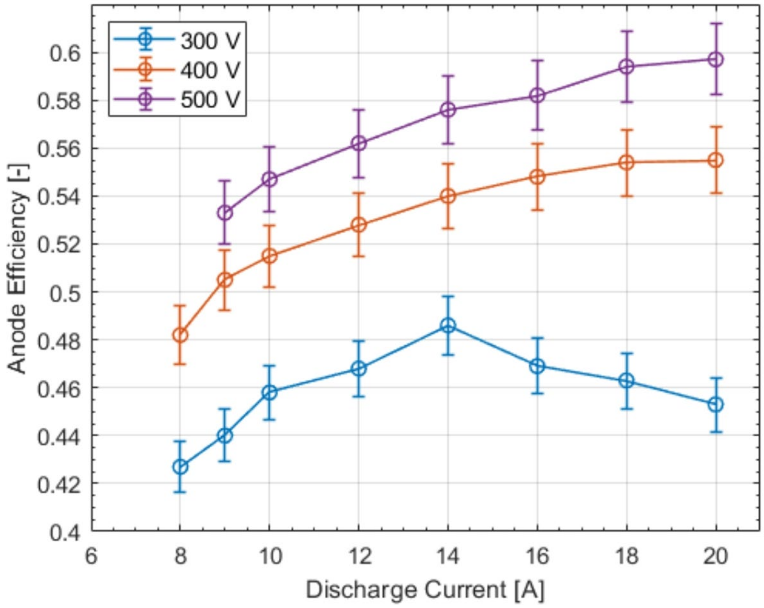

Fig. 5 Anode efficiency as a function of discharge current for discharge voltages of 300 V, 400 V, and 500 V

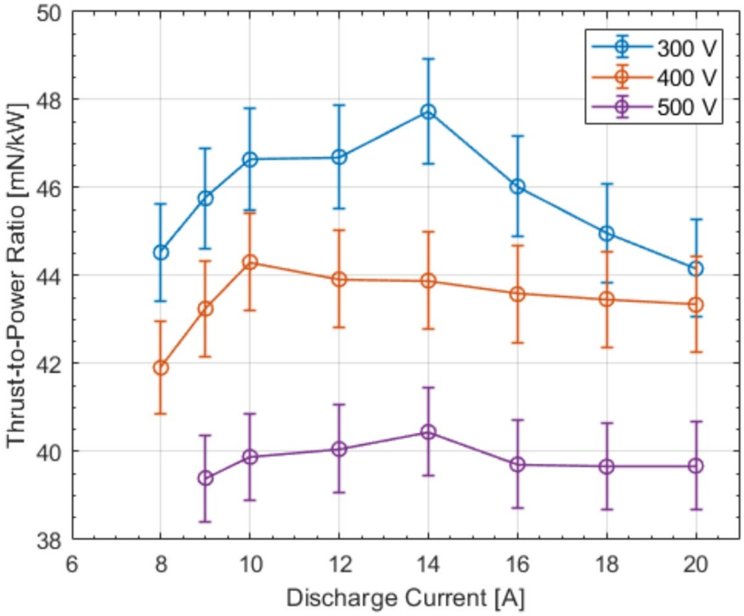

Fig. 6 Thrust-to-power ratio as a function of discharge current for discharge voltages of 300 V, 400 V, and 500 V

faraday current also exhibits a sharper off-axis decrease as discharge current increases. Interestingly, the measured faraday current also exhibits an asymmetry in its peak that becomes more pronounced with increasing discharge current. The asymmetry in the T-140 plume has been observed previously and can potentially be attributed to asymmetries in the B-field topology [8]. As the discharge current increases, the acceleration region is pushed further downstream into regions with potentially larger asymmetries in the B-field topology [5, 26]. Having the bulk of the acceleration occur in a region of greater B-field asymmetries could explain why the measured current in the plume is more asymmetric.

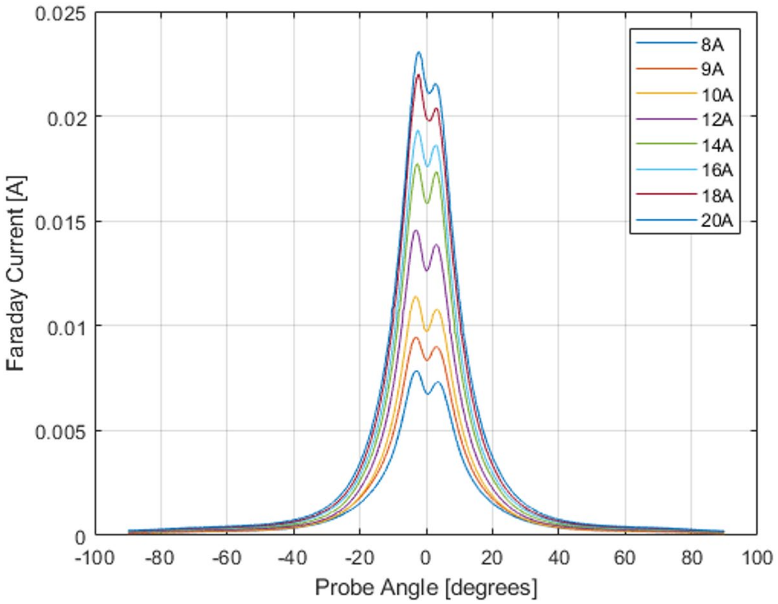

Fig. 7 Raw Faraday probe trace for 300 V discharge condition for discharge currents of 8–20 A on krypton

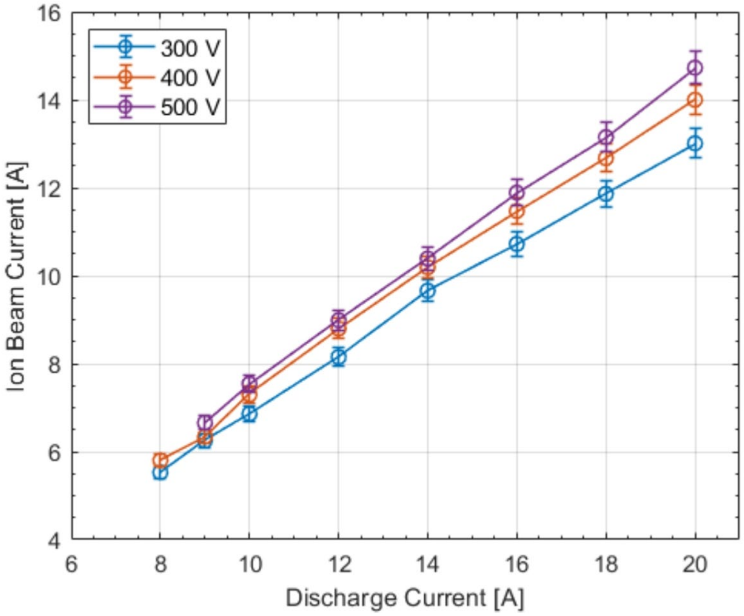

Fig. 8 Beam current as a function of discharge current for discharge voltages of 300 V, 400 V, and 500 V

The beam current exhibits an approximately linear trend with discharge current, before slightly beginning to asymptote at higher discharge currents. The beam current also slightly increases with discharge voltage, which agrees with previous studies [21]. This increase is attributed to the increase in electron energy with discharge voltage. Increasing the discharge voltage increases the electric field strength, thus accelerating the electrons to higher energies [20, 22]. The higher electron energy increases

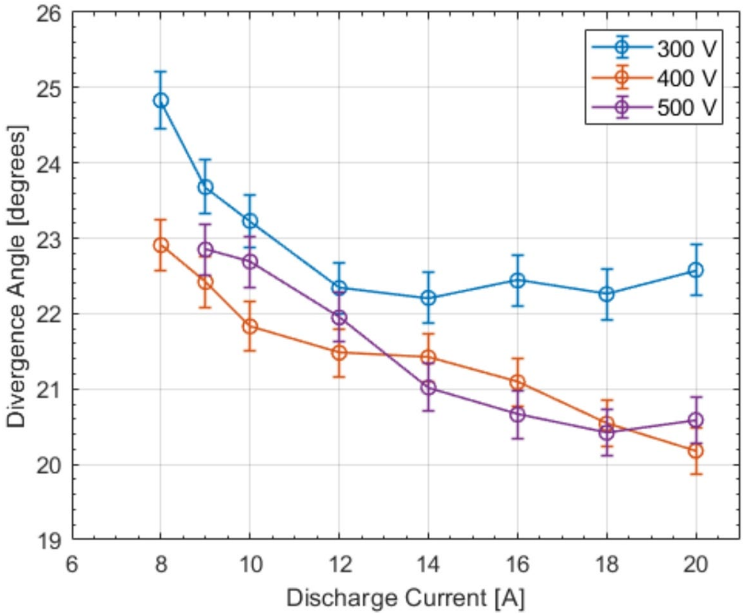

Fig. 9 Divergence angle as a function of discharge current for discharge voltages of 300 V, 400 V, and 500 V

the ionization rate, leading to the higher beam current at higher discharge voltages as observed in this test [21, 23].

The divergence angle decreases with increasing discharge current before reaching an asymptote. One potential reason behind the measured behavior is a possible decrease in electron temperature with increased neutral and plasma density. The higher discharge currents are achieved by flowing more neutral propellant, which would lead to a higher electron collision frequency, thus potentially quenching the electrons to a lower mean energy. This is consistent with the works of Fossum et al. which found that increasing the neutral density in an ExB device led to a decrease in electron temperature due to the aforementioned collisional quenching mechanism [24]. The electron temperature plays an important role in the motion of ions, which travel towards the wall sheath at the Bohm velocity, which is proportional to the square of the electron temperature as seen in Eq. (15) [5, 20, 21].

$$v_B = \sqrt{\frac{q_e T_e}{m_i}} \tag{15}$$

Where v_B is the Bohm velocity and T_e is the electron temperature in eV. Decreasing the electron temperature would decrease the ions' radial motion thus decreasing the divergence angle. However, increasing the discharge current also pushes the acceleration region further downstream the axial channel of the Hall thruster, which has been shown to increase divergence angle [5, 25, 26]. The decrease in electron temperature with increasing neutral density follows an exponential decay, trending towards an asymptote at higher neutral densities [24]. This, combined with the competing effect of pushing the acceleration region downstream, could potentially explain the asymptotic behavior of the divergence angle seen at higher discharge currents.

The measured divergence angle also decreases with the discharge voltage. This matches previous studies, which attributed the decrease in divergence angle to the discharge voltage increasing faster than the increase in electron temperature [21]. Ions are accelerated axially out of the thruster by the potential difference between the cathode and the anode and travel towards the wall sheath, as mentioned previously, at the Bohm velocity [20, 21]. Increasing the discharge voltage faster than the electron temperature leads to a greater axial motion relative to the motion towards the walls leading to a smaller divergence angle [21].

The RPA was used to characterize the most probable acceleration voltage and the results are presented in Fig. 10 with the discharge voltages denoted with dashed lines for reference. The accelerating voltage was found to remain relatively constant with discharge current and increase, as expected, with discharge voltage.

Efficiency breakdown analysis

The probe measurements outlined in the previous section were used to calculate and analyze the efficiency breakdown using the framework outlined in Sec. III.B to gain a better understanding of trends seen in the global performance measurements, specifically the anode efficiency. The voltage utilization, calculated based on the RPA measurements, is presented in Fig. 11.

The voltage utilization shows no clear trend and remains relatively constant with discharge current. This agrees with previous measurements of voltage utilization for high current density operation for krypton [5]. Meanwhile, the voltage utilization slightly increases with discharge voltage, with the mean voltage drop decreasing from approximately 28 V at the 300 V discharge condition to 21 V at the 500 V discharge condition. This is consistent with the works of Hofer et al., who found a similar drop in ion loss voltage with increasing discharge voltage [13]. The voltage utilization efficiency defined in Eq. (5) can be defined in terms of the ion loss voltage, V_I, the difference between the discharge voltage and the measured most probable voltage:

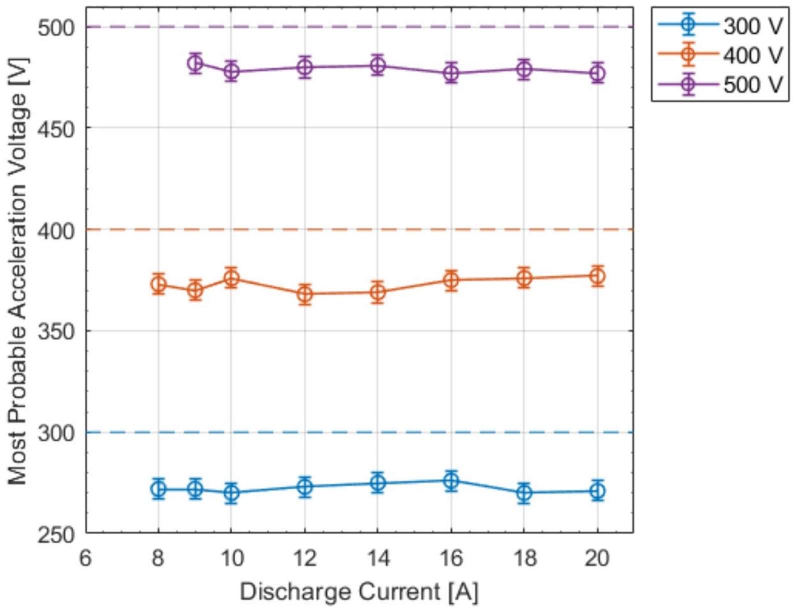

Fig. 10 Most probable accelerating voltage as a function of discharge current for discharge voltages of 300 V, 400 V, and 500 V

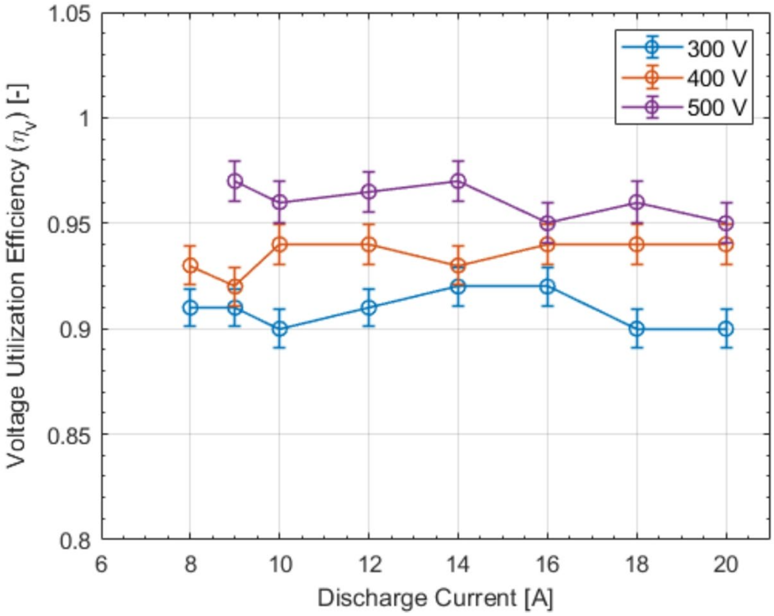

Fig. 11 Voltage utilization efficiency (η_v) as a function of discharge current for discharge voltages of 300 V, 400 V, and 500 V

$$\eta_v = \frac{V_a}{V_d} = 1 - \frac{V_I}{V_d} \tag{16}$$

This ion loss voltage can be attributed to the potential difference needed to accelerate electrons from the cathode and the formation of a fraction of the ions downstream of the peak electric field which lead to a lower acceleration of those ions. The former is dependent on the cathode emitter material and design and is not affected by discharge voltage, while the effect of the latter decreases slightly as the discharge voltage increases, shifting the region of ionization upstream [27]. As such increasing the discharge voltage should decrease the ion loss voltage, as seen in the measurements, and thus increase the voltage utilization efficiency.

The current utilization efficiency, calculated based on Faraday probe measurements, is presented in Fig. 12.

The current utilization efficiency is the lowest component efficiency suggesting that it has the greatest effect on the measured anode efficiency behavior. Furthermore, the trends in current utilization efficiency match those of the anode efficiency. The current utilization efficiency shows a peak between 12 and 14 A for all three discharge voltage conditions with the current peak becoming less prominent with increasing voltage. There are two possible competing effects that could affect the current utilization efficiency as the discharge current is increased. On the one hand, increasing the discharge current through increased mass flow initially increases the amount of ionization leading to more ions in the plume, as seen by the beam current measurements in Fig. 8. This increase in beam current occurs faster than the increase in discharge current, which in turn increases the current utilization. On the other hand, increasing neutral density increases electron collisionality, which in turn increases electron cross-field mobility [24, 28]. This increase in cross-field mobility would, in turn, increase the discharge current faster than the beam current and lead to a decreasing current utilization efficiency. At

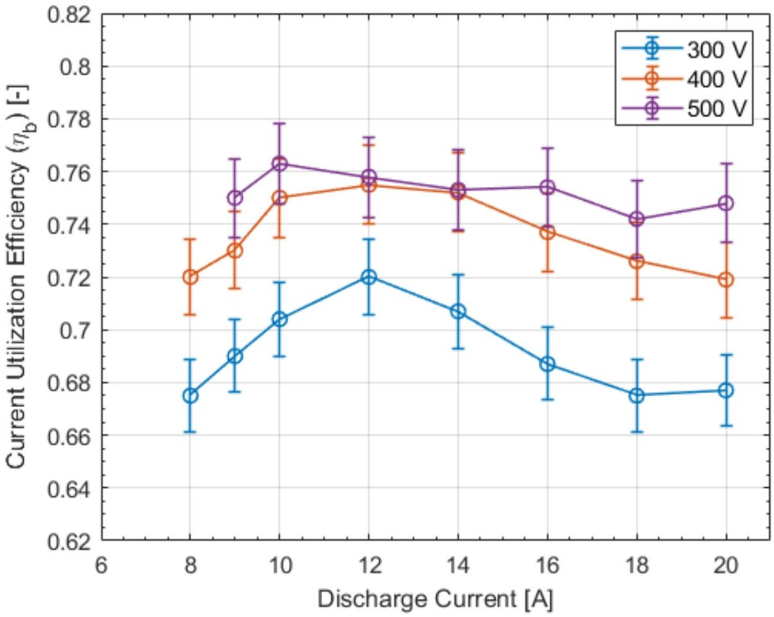

Fig. 12 Current utilization efficiency (η_b) as a function of discharge current for discharge voltages of 300 V, 400 V, and 500 V

some point, the increase in ionization will saturate and the increase in cross-field mobility will dominate, potentially explaining why there is a peak efficiency, after which the current utilization decreases with further increases in discharge current. The increase in current utilization with discharge voltage can be attributed to the increase in electron energy, which would increase the overall ionization rate, thus increasing the current utilization [20]. This increase in electron temperature would also increase the fraction of electron-neutral collisions that lead to ionization as opposed to other interactions such as excitation [29]. This would mean that the increased electron collisionality with increasing discharge current, which decreases current utilization, comes with more ionization at higher voltages, which increases current utilization efficiency, possibly providing an explanation for the shallower decrease in current utilization beyond the peak at higher discharge voltages.

The divergence efficiencies, calculated based on the divergence angle measurements from the Faraday probe, as described in Eq. (7), are presented in Fig. 13.

The divergence efficiency increases with decreasing divergence angle and as such follows the inverse trend of the divergence angle, increasing with discharge current before reaching an asymptote. Given that the divergence efficiency is dependent only on the divergence angle, the same explanations for the trends in the divergence angle discussed in the previous section determine the trends seen in Fig. 13.

The mass utilization efficiency, calculated based on Faraday probe measurements and input mass flow rate, is presented in Fig. 14.

The mass utilization efficiency increases with discharge current before beginning to asymptote. Similar trends have been measured for high current density operation for both krypton and xenon [5]. This trend can be attributed to a decreasing ionization mean free path, which is inversely proportional to plasma density, leading to a higher ionization fraction and hence an increasing mass utilization [30]. The asymptotic behavior suggests that the ionization process begins to saturate as most of the neutral gas is

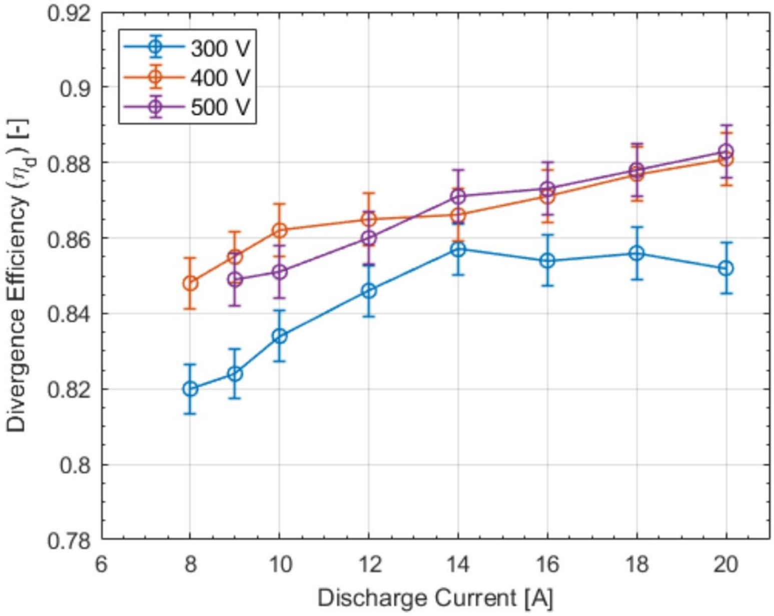

Fig. 13 Divergence efficiency (η_d) as a function of discharge current for discharge voltages of 300 V, 400 V, and 500 V

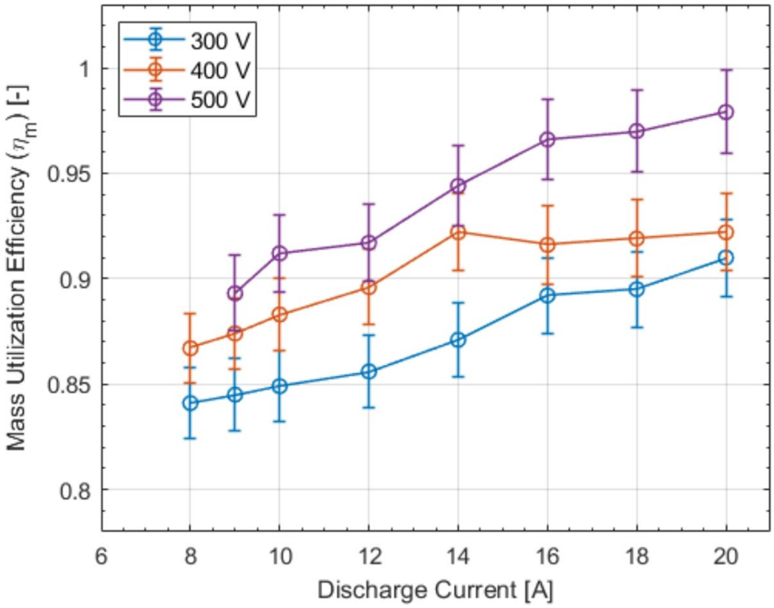

Fig. 14 Mass utilization efficiency (η_m) as a function of discharge current for discharge voltages of 300 V, 400 V, and 500 V

ionized at the higher current densities, matching the theory discussed for the current utilization trends. As seen in Eq. (14), the specific impulse is proportional to the mass utilization efficiency. The mass utilization efficiency begins its asymptotic behavior at approximately 16A, which, given the aforementioned proportionality, explains the asymptotic behavior in the specific impulse, as previously postulated, which also starts at around 16 A. The mass utilization also increases with discharge voltage which can be attributed to more ionization due to the higher electron temperature.

It is important to note that the probe-based efficiency calculations, especially the mass utilization efficiency, may be slightly overestimated due to assuming singly charged ions as Faraday probe measurements of a multi-charged ion and multiple singly charged ions cannot be distinguished from each other. This error is expected to be larger at higher discharge voltages as there will be a higher fraction of multi-charged ions [20]. To assess the extent of this error, the anode efficiency calculated based on the probe decomposition is compared to the calculations based on the global thrust measurements and presented in Fig. 15 for the three voltage conditions.

As theorized, the error between the anode efficiency calculated using measured thrust and estimated using the probe decomposition increased with discharge voltage, suggesting that neglecting multi-charged ions may be the main source of error in the probe estimation method. However, the differences between the two methods are within the uncertainty for all setpoints and the results show the same trends. Thus, the implications and conclusions drawn from the efficiency decomposition analysis are still believed to be valid.

Thruster body temperature

The thruster body temperature measurements are presented in Fig. 16.

The thruster body temperature increases approximately linearly with discharge current, but only slightly increases with discharge voltage. This is interesting as it suggests that the body temperature is predominantly a function of discharge current as opposed to discharge power. For example, comparing the 300 V, 20 A and 500 V, 20 A conditions, which correspond to 6 and 10 kW respectively, the temperature increases by 8° C. However, comparing the 500 V, 12 A and 500 V, 20 A conditions, which also correspond 6 and 10 kW respectively, the temperature increases by 32° C. The increase in thruster body temperature can be predominantly attributed to energy deposition from ion-wall and electron-wall collisions [20]. Increasing the discharge current density will increase the plasma density in the channel leading to a higher number of collisions

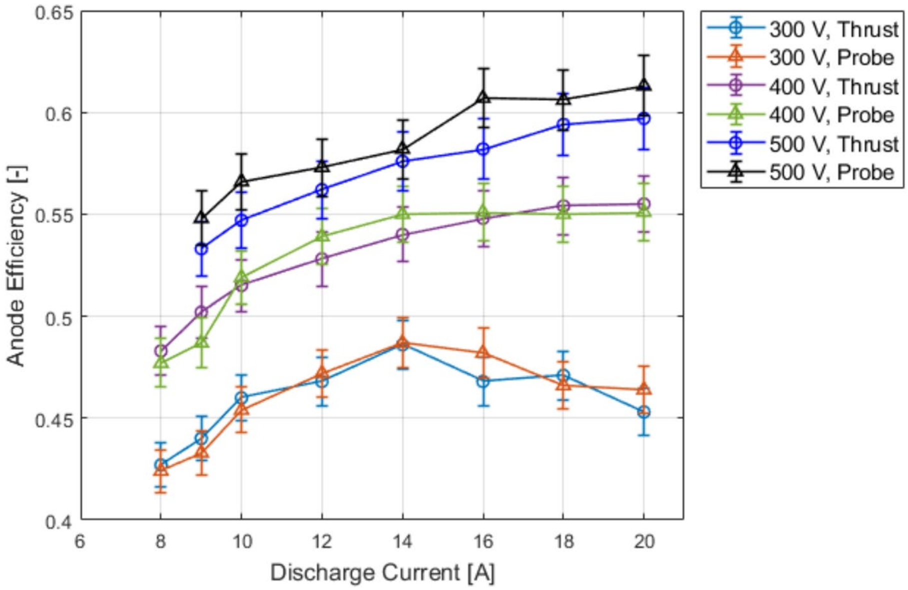

Fig. 15 Comparison of anode efficiency calculated from thrust and from probes for 300, 400, and 500 V discharge conditions

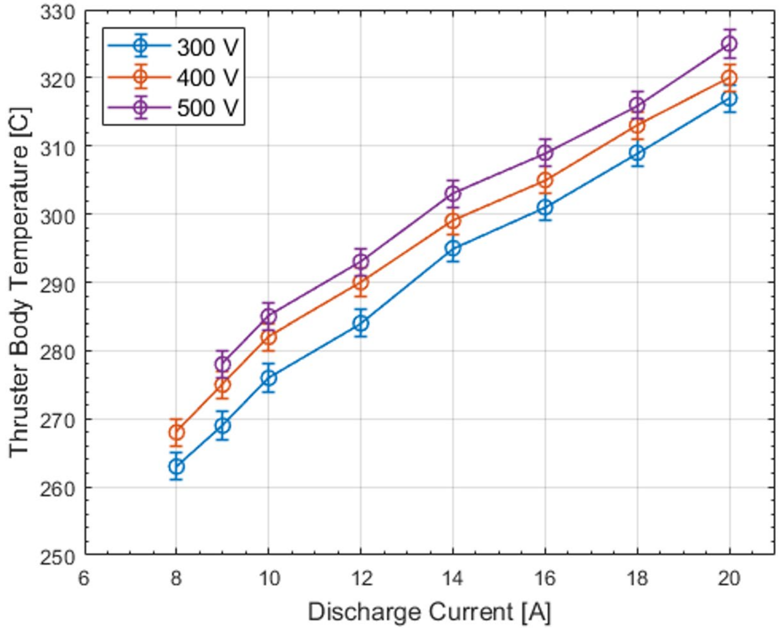

Fig. 16 Thruster body temperature for 300, 400, and 500 V discharge conditions

hence explaining the linear trend with discharge current. The trends with discharge voltage, on the other hand, contradict what is expected from previous works, which have shown a linear trend with voltage at lower discharge voltages and an exponential trend at higher discharge voltages [31]. However, it is important to note that the trends presented in Fig. 16, are based on a single temperature measurement on the outside of the thruster body. As such, a much more in-depth analysis with measurements at multiple locations on the thruster are needed to understand why the trend with discharge voltage does not match previous work.

Scaling laws and nondimensional analysis

The following section presents a comparison between the results obtained in this investigation and scaling laws and non-dimensional analysis derived in previous works. While most scaling laws and non-dimensional analysis focus on size scaling of HETs, there have been some works that also analyzed the power scaling as well. The work of Shagayda et al. derived an approximation for the mass utilization efficiency assuming that ion loss to the walls was negligible, wall and ion temperatures are constant, and that heat transfer from the channel walls to propellant neutrals is purely radiative [32]:

$$\eta_m = 1 - \exp\left(-C\frac{m_p\beta_i\sqrt{P_d}}{V_d}\eta_b\right) \tag{17}$$

Where β_i is the ionization reaction rate, P_d is the discharge power, and C is a proportionality constant. An experimental analysis done on various HETs operating from 0.3 to 3 kW found that the value of C had very little variation around an average value of approximately 1.3 10^{12} [32]. Values of β_i were estimated by assuming that the electron temperature was 10% of the discharge voltage, which is a common assumption employed in previous works [20]. The works of Shagayda et al. estimated the scaling of anode efficiency using the approximation in Eq. (17) and experimentally derived values of voltage, divergence, current and charge efficiencies [32]. Doing a similar analysis under the same assumptions yields the results shown in Fig. 17.

While the scaling law underestimates the anode efficiency, it manages to capture the overall trend with discharge current and voltage, including the location of the peak discharge current at 14 A for the 300 V condition, showing good agreement between the scaling law and the experimental data. It is important to highlight that assuming a constant C-coefficient is equivalent to assuming the same heat flux to/from the walls of the discharge channel [32]. However, it is expected that, for a given thruster geometry, at higher discharge powers, there would be greater heat flux to the walls. This could explain why the difference between the measured and modeled efficiencies becomes very large at very low and very high discharge powers where the heat flux is expected to be the most disparate. Despite this, the model still captures the trends in anode efficiency well suggesting that changes in the heat flux do not affect the scaling trends with power despite affecting the actual predicted values of anode efficiency.

In the work of Lafleur et al., a set of 1D non-dimensional forms of the continuity and momentum conservation equations were derived, and the anode efficiency was derived in terms of the non-dimensional momentum flux [33]:

$$\eta_T = \left(\frac{m_p \in_{iz} I_d}{2 q_e \dot{m}_a V_d}\right)\bar{G}_L^2 \tag{18}$$

$$\bar{G}_L = \left(\frac{n_i v_i^2}{v^* \Gamma_\mathrm{d}}\right) \tag{19}$$

$$\Gamma_D = \left(\frac{I_d}{q_e A_{ch}}\right) \tag{20}$$

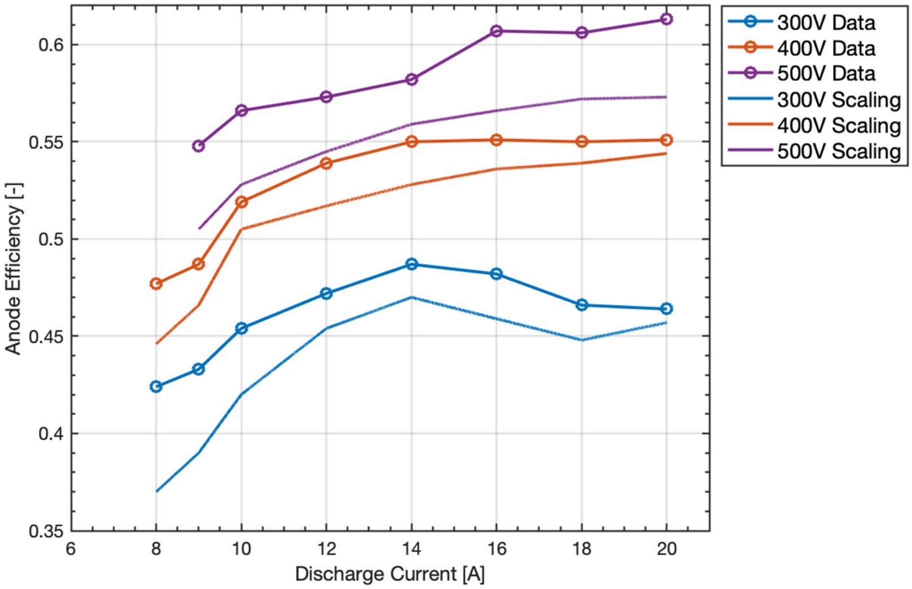

Fig. 17 Comparison of anode efficiency calculated from experiment and calculated from mass efficiency estimate from scaling laws

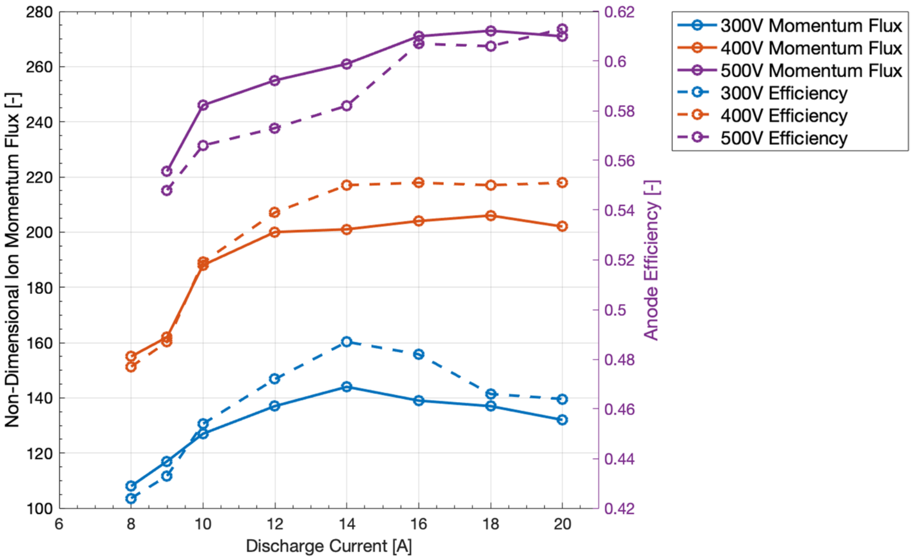

Fig. 18 Non-dimensional ion momentum flux based on centerline probe measurements

$$v^* = \sqrt{\left(\frac{q_e \in_{iz}}{m_p}\right)} \tag{21}$$

Where $\bar{G}_L$ is the non-dimensional ion momentum flux, n_i is the ion density, Γ_D is the charge flux of the discharge, v_i is the ion velocity, v^* is a characteristic velocity, $\in_{iz}$ is the ionization energy, and A_{ch} is the discharge channel area. The non-dimensional ion momentum flux was estimated based on centerline probe measurements and plotted in Fig. 18 alongside the anode efficiency for reference.

The trends in the non-dimensional ion momentum flux follow the same trends with discharge current and voltage as the anode efficiency including portraying a peak at 14 A for the 300 V discharge condition. This allows us to understand the trends in anode efficiency from a different perspective. As seen in Eq. (19), the momentum flux is non-dimensionalized by the total ion flux in the discharge times a characteristic velocity calculated based on the ionization energy, which is constant for a given propellant. As such, changes in the non-dimensional momentum flux, and by extension, the anode efficiency can be attributed to the changes in the ion momentum flux leaving the thruster relative to changes in the total ion flux in the discharge. This represents a physical mechanism very similar to that which is captured by the current utilization efficiency, thus affirming our conclusion that it is the dominant efficiency in determining the total anode efficiency trends.

Conclusion

The high current density operation of a 4.5 kW Hall effect thruster was characterized at power levels up to 10 kW on krypton for three discharge voltage conditions: 300, 400, and 500 V with a focus on the trends in anode efficiency. It was found that the 300 V condition exhibited a peak efficiency at 14 A with increasing discharge current, while the 400 and 500 V conditions did not exhibit a peak within the range of discharge currents analyzed and instead increased asymptotically with discharge current. By decomposing the anode efficiency into its constituent efficiencies, it was found that the current utilization efficiency was the lowest efficiency, suggesting that it had the highest contribution to the measured anode efficiency behavior. Furthermore, the trends in current utilization efficiency matched those of the anode efficiency. These trends with discharge current are attributed to a balance between increasing ionization and increasing cross-field mobility with increasing discharge current. The current utilization efficiency was also found to increase with discharge voltage. This trend is attributed to the higher electron temperature at higher discharge voltages which increases ionization. The mass utilization and divergence efficiencies were also found to vary significantly with both discharge voltage and current, while the voltage utilization showed little change with discharge voltage and no discernible trend with discharge current. Neglecting multi-charge ions was identified as a potential source of error, but a comparison between anode efficiency measurements based on thrust and the estimated anode efficiency based on plume measurements showed that the differences between the two methods were within the uncertainty for all setpoints giving confidence in the analysis methods employed.

This work provides a good further step in understanding high current density operation of HETs in order to obtain high thrust density operation for deep space missions and other applications. This work expands upon previous investigations, which focused on the efficiency trends with increasing current density of a magnetically shielded thruster, by exploring these same trends on an unshielded thruster and focusing on how these trends change with changing discharge voltage. However, there are multiple avenues of further research to build upon this work. For this work, the magnetic field was kept constant for all setpoints. It would be beneficial to study how the optimum B-field changes with high current density operation at varying voltages and the effect, if any, that varying the B-field would have on the efficiency trends. It would also be interesting to study and compare high current density operation on lighter propellants such as argon or even molecular propellants such as N_2/O_2 mixtures or CO_2. Lighter propellants can provide higher I_{sp} operation and molecular propellants such as N_2/O_2 mixtures have become of great interest for air-breathing EP applications. Despite this, HETs operating on these propellants have shown lower efficiencies when compared to more traditional propellants such as krypton and xenon [34, 35]. However, initial experimental work comparing HET operation on xenon, krypton, argon, and nitrogen has shown that at high current densities, the mass utilization of the different propellants converged [36]. As such, it is possible, that HETs can become propellant agnostic and operate with a wide range of propellants with comparable performance at higher current densities. However, further investigation is still needed to understand the effect of high current density operation on overall efficiency for a wide variety of propellants at a larger range of discharge conditions. It would also be useful to investigate a direct comparison of the high current density performance of the magnetically shielded and unshielded configurations of the same thruster with a focus on current oscillations. This may grant some insight on the differences seen in the stability criterion for the two configurations at high voltages and how that criterion changes with increased current density for krypton operation [37, 38].

Nomenclature

A_{ch}	Discharge channel area
A_{en}	Neutral ingestion entrainment area
C	Proportionality constant
k_b	Boltzmann's constant
G_L	Non-dimensional ion momentum flux
g_o	Standard gravity

I_b	Ion beam current
$I_{b,corr}$	Corrected ion beam current
I_d	Discharge current
$I_{d,corr}$	Corrected discharge current
I_{sp}	Specific Impulse
m_i	Propellant ion mass
m_p	Propellant atom mass
$\dot{m}$	Total mass flow rate
$\dot{m}_a$	Anode mass flow rate
$\dot{m}_b$	Ion beam mass flow rate
$\dot{m}_{en}$	Entrained neutral mass flow rate
n_i	Ion density
p	Chamber operating pressure at a given setpoint
P_d	Discharge power
q_e	Elementary electron charge
T	Thrust
T_{corr}	Corrected thrust
T_e	Electron Temperature in eV
T_o	Neutral gas temperature
V_a	Ion accelerating voltage
V_d	Discharge voltage
V_I	Ion loss voltage
v_B	Bohm velocity
v_i	Ion velocity
v^*	Characteristic velocity
Z_i	Charge of the ith ion species
β_i	Ionization reaction rate
$\in_{iz}$	Ionization energy
Ω_i	Current fraction of the ith ion species
η_a	Anode efficiency
η_q	Charge utilization efficiency
η_ν	Voltage efficiency
η_b	Current utilization efficiency
η_m	Mass utilization efficiency
θ_{div}	Divergence angle
ζ_A	Area entrainment correction factor
ζ_{en}	Thrust entrainment correction factor

Acknowledgements
My fellow graduate students at HPEPL for helping me bounce ideas around and offering writing advice.

Author contributions

M.E., C.C., M.L.R.W, D.L. and B.N. were responsible for conceptualization of the experiment and defining the scope. Material collection, experimental setup and data collection were conducted by M.E. and N.M. Data analysis and organization was conducted by M.E, C.C., and N.M. The original paper draft was written by M.E. and N.M. and was edited by all authors. M.L.R.W., D.L., B.N., A.C., and S.S. were responsible for project administration. All authors read and approved the final manuscript.

Funding
This publication is based on work supported by Lockheed Martin. Any opinions, findings, conclusions or recommendations expressed in this publication are those of the authors and do not necessarily reflect the views of Lockheed Martin.

Data availability

No datasets were generated or analysed during the current study.

Declarations

Competing interests

The authors declare no competing interests.

Received: 8 October 2025 / Accepted: 1 March 2026

References

1. Jovel D, Walker R, M. L. R., and, Herman D (November-December 2022) Review of high-power electrostatic and electrothermal electric propulsion. J Propul Power 38(6). https://doi.org/10.2514/1.B38594
2. Surampudi R, Blosiu J, Stella P, Elliot J, Castillo J, Yi T, Lyons J, Piszczor M, McNatt J, Taylor C, Gaddy E, Liu S, Plichta E, Iannello C, Beauchamp P, Cutts JA (Dec 2017) Solar power technologies for future planetary science missions, NASA/Jet Propulsion Lab. Rept. JPL D-101316.

3. Simmonds J, Raitses Y, Smolyakov A (March 2023) A theoretical thrust density limit for Hall thrusters. J Electric Propul 2(2). https://doi.org/10.1007/s44205-023-00048-9
4. Liang R (2013) The Combination of two concentric discharge channels into a nested Hall-effect thrust. PhD. Dissertation, University of Michigan, Ann Arbor, MI
5. Su LL, Roberts PJ, Gill TM, Hurley WJ, Marks TA, Sercel CL, Allen MG, Whittaker CB, Viges E, Jorns BA (May 2024) High-current density performance of a magnetically shielded Hall thruster. J Propul Power 40(3). https://doi.org/10.2514/1.B39324
6. Lev DR, Lev, Franco DK, Auslender B and Epstein O (2022) Extension of the operation envelope of the R-200 low power Hall thruster. In: 37th International electric propulsion conference, IEPC-2022-357, Boston, Massachusetts. https://doi.org/10.2514/1.B39324
7. McLean CH, McVey JB, Schappell DT (1999) Testing of a U.S.- Built HET system for orbit transfer applications, 35th AIAA/ASME/SAE/ASEE Joint propulsion conference and exhibit. AIAA-99-2574, Los Angeles, California
8. Jonathan AW (2016) Electrical facility effects on Hall effect thruster operation, Dissertation PD Aerospace Dept., Georgia Institute of Technology. Atlanta; Georgia
9. Polk JE, Pancotti A, Haag T, King S, Walker M, Blakely J, Ziemer J (2013) Recommended practices in thrust measurements. In: 333rd International electric propulsion conference. IEPC-2013-440, Washington, DC
10. Lobbia RB, Beal BE (May-June 2017) Recommended practice for use of langmuir probes in electric propulsion testing. J Power Propuls 33(3). https://doi.org/10.2514/1.B35531
11. Hofer RR, Walker MLR, Gallimore A (2001) A comparison of nude and collimated faraday probes for use with Hall thrusters. In: 27th International electric propulsion conference, IEPC-01-020, Pasadena, California
12. Brown DL, Walker MLR, Szabo J, Huang W, Foster JE (May-June 2017) Recommended practice for use of Faraday probes in electric propulsion testing. J Propul Power 33(3). https://doi.org/10.2514/1.B35696
13. Hofer RR, Gallimore AD (July-August 2006) High-specific impulse Hall thrusters, part 2: efficiency analysis. J Propul Power 22(4). https://doi.org/10.2514/1.15954
14. Randolph T, Kim V, Kaufman H, Kozubsky K, Day M (1993) Facility effects on stationary plasma thruster testing, 23rd International electric propulsion conference. Seattle, Washington
15. Brown DL (2009) Investigation of low discharge voltage Hall thruster characteristics and evaluation of loss mechanisms. PhD. Dissertation, University of Michigan, Ann Arbor, MI
16. Reid BM (2009) The influence of neutral flow rate in the operation of Hall thrusters. PhD. Dissertation, University of Michigan, Ann Arbor, MI
17. Hofer RR, Gallimore AD (2003) Recent results from internal and very-near-field plasma diagnostics of a high specific impulse Hall thruster. In: 28th International electric propulsion conference. Toulouse; France
18. Azziz Y (2007) Experimental and theoretical characterization of a Hall thruster plume. PhD. Dissertation, Massachusetts Institute of Technology. Boston; MA
19. Huang W, Kamhawi H, Herman DA (2018) Ion velocity in the discharge channel and near-field of the HERMeS Hall thruster. 2018 Joint propulsion conference. AIAA-2018-4273, Cincinnati, Ohio
20. Goebel DM, Katz I (2008) Fundamentals of electric propulsion. Ion and Hall thrusters, Wiley
21. Azziz Y, Martinez-Sanchez M, Szabo JJ (2005) Effect of discharge voltage on plume divergence of a high specific impulse Hall thruster. In: 41st AIAA/ASME/SAE/ASEE joint propulsion conference and exhibit. Tucson; Arizona
22. Zhurin VV, Kaufman HR, Robinson RS (January, 1999) Physics of closed drift thrusters. Plasma Sources Sci Technol 8(1). https://doi.org/10.1088/0963-0252/8/1/021
23. Su LL, Marks TA, Jorns BA (June, 2024) Trends in mass utilization of a magnetically shielded Hall thruster operating on xenon and krypton. Plasma Sources Sci Technol 33(6). https://doi.org/10.1088/1361-6595/ad52be
24. Fossum EC, King LB (2008) Effects on neutral density on electron temperature and mobility in a crossed-field trap. In: 44th AIAA/ASME/SAE/ASEE Joint propulsion conference and exhibit. Hartford; Connecticut. https://doi.org/10.2514/6.2008-5190
25. Nakles MR, Hargus WA Jr. (2011) Background pressure effects on ion velocity distribution within a medium-power Hall thruster. J Propul Power 27(4):737–743. https://doi.org/10.2514/1.48027
26. Cusson SE, Dale ET, Jorns BA, Gallimore AD (2019) Acceleration region dynamics in a magnetically shielded Hall thruster. Phys Plasmas 26(2). https://doi.org/10.1063/1.5079414
27. Zheng Y, Zhang W, Li M, Li Z, Wang Y (2023) Study on the influence of discharge voltage on the performance of Hall propulsion system. AIP Adv 13(10). https://doi.org/10.1063/5.0173717
28. Dannenmayer K, Mazouffre S (2011) Elementary scaling relation for Hall effect thrusters. J Propul Power 27(1). https://doi.org/10.2514/1.48382
29. Hara K (2019) An overview of discharge plasma modeling for Hall effect thrusters. Plasma Sources Sci Technol 28(4). https://doi.org/10.1088/1361-6595/ab0f70
30. Ashkenazy J, Raitses Y, Appelbaum G (May 1998) Parametric studies of the Hall current plasma thruster. Phys Plasmas 5(5) https://doi.org/10.1063/1.872877
31. Mazouffre S, Dannenmayer K, Blank C (2011) Impact of discharge voltage on wall-losses in a Hall thruster. Phys Plasmas 18(6). https://doi.org/10.1063/1.3592251
32. Shagayda AA, Gorshkov OA (2013) Hall-thruster scaling laws. J Propul Power 29(2). https://doi.org/10.2514/1.B34650
33. Lafleur T, Chabert P (2025) Similarity parameters and scaling laws for Hall thrusters. Plasma Sources Sci Technol 34(5). https://doi.org/10.1088/1361-6595/add562
34. Lee D, Brabston WP, Lev D, Walker MLR (2024) Argon admixture-driven enhanced ionization and performance of a 5 kW Hall thruster on krypton. J Phys D 57(32) https://doi.org/10.1088/1361-6463/ad4562
35. Brabston WP, Marino LA, Lev D, Walker MLR (2024) Analysis of the ionization and acceleration efficiencies of molecular nitrogen in a Hall effect thruster. In: 38th international electric propulsion conference, IEPC-2024-297. Toulouse; France
36. Hurley WJ, Jorns BA (May 2025) Mass utilization scaling with propellant type on a magnetically shielded Hall thruster. Plasma Sources Sci Technol 34(5). https://doi.org/10.1088/1361-6595/add61e
37. Jorns BA, Dale E, Hofer RR (August 2024) Mode transitions in a magnetically shielded Hall thruster. I. Experimentally informed model. J Appl Phys 136(5) https://doi.org/10.1063/5.0205983

38. Jorns BA, Byrne M, Roberts P, Dale SL, Hofer RR (August 2024) Mode transitions in a magnetically shielded Hall thruster. II. stability criterion. J Appl Phys 136(5) https://doi.org/10.1063/5.0205985

Publisher's note